100 kHz High-Spectral-Resolution NO-PLIF Measurements for Compressible Flows

Neil S. Rodrigues[1], Paul M. Danehy[2]
NASA Langley Research Center, Hampton, VA, 23666, United States

Naibo Jiang[3], Paul Hsu[4], Jason Leicht[5], Sukesh Roy[6]
Spectral Energies, LLC, Dayton, OH, 45430, United States

In the present work, we use a burst-mode laser and optical parametric oscillator system to perform high-spectral resolution NO-PLIF measurements of an underexpanded jet at a repetition-rate of 100 kHz, with the motivation of multi-parameter measurements of temperature, pressure, and velocity. The laser frequency of the 1064 nm seed laser for the burst-mode laser was scanned during the burst to cover two neighboring absorption line pairs near 226 nm. The peak PLIF signal intensity varies along the axial (*z*) direction of the underexpanded jet as the laser frequency is scanned, which we attribute to the collisional shift induced by the flow and only revealed due to the narrow linewidth of the laser. A pseudo-Voight fit is applied to the LIF excitation spectra on a pixel-by-pixel basis to measure the spectral position of the peak intensity for the two transition pairs and their amplitude. The spectral position of the peak intensity is used to derive a frequency shift, which is separated into its collisional and Doppler components using the axisymmetric nature of the flow field. The amplitude of the measured peaks is used for two-line rotational thermometry. Challenges for quantitative measurements using such an approach are discussed, including measuring the spatial variations in the energy distribution of the laser sheet at a 100 kHz repetition rate and uncertainty/variability in the step size during the fast frequency scan.

I. Introduction

Non-intrusive, multi-parameter flow measurements are highly desirable for the compressible flow fields found within supersonic and hypersonic wind tunnels in order to provide validation data for simulations using computational fluid dynamics (CFD). Planar laser-induced fluorescence (PLIF) is one of several non-intrusive measurement techniques that have been commonly used within wind tunnel facilities [1]. PLIF measurements of the nitric oxide (NO) molecule, which is either premixed with the wind tunnel test fluid, locally injected, or naturally present, for example in arc-heated and shock-heated facilities, is typically performed using the A-X electronic system, with the majority of studies using ($v' = 0$, $v'' = 0$) excitation near 226 nm. NO-PLIF experiments have traditionally been performed using an Nd:YAG pumped dye laser system at a laser repetition-rate of 10 Hz. However, such systems usually feature a laser linewidth that is greater or comparable with the linewidth of the NO absorption transition. Extending NO-PLIF measurements to kHz-MHz rates pose additional complexities. Most recently, Jiang *et al.* [2] performed MHz rate NO-PLIF flow visualization using a burst-mode laser and optical parametric oscillator (OPO) system within a Mach 10 shock tunnel. While comparisons between the experimental PLIF intensity and a simulated PLIF image using a *computational flow imaging* approach are possible [3], quantitative interpretations of PLIF measurements performed within compressible flow fields at large-scale ground test facilities are challenging due to effects of laser absorption and saturation [4].

On the other hand, high-spectral-resolution laser-induced fluorescence (LIF) can be used to measure thermodynamic and flow parameters that can be directly compared with CFD results. High-spectral-resolution LIF

[1] Optical Physicist, Advanced Measurements and Data Systems Branch, AIAA Member.
[2] Senior Technologist, Advanced Measurements and Data Systems Branch, AIAA Associate Fellow.
[3] Senior Research Scientist, AIAA Associate Fellow.
[4] Senior Research Scientist, Senior Member AIAA.
[5] Research Scientist, AIAA Member.
[6] Senior Research Scientist and CEO, AIAA Associate Fellow.

measurements for multi-parameter flow measurements were first demonstrated by Zimmerman and Miles using vapor-phase sodium [5]. In the following years, high-spectral resolution LIF was performed by McDaniel *et al.* using iodine [6] and DiRosa *et al.* using nitric oxide) [7]. In these earlier studies, measurements were performed using a relatively low intensity continuous wave (CW) laser and the measurements were therefore limited to a single point. While dye laser systems, such as the one used by Danehy *et al.* [8], can provide the high laser intensity needed for two-dimensional (2D) measurements, they generally feature relatively broad laser linewidths, on the order of 0.1 cm^{-1}, which is greater or comparable with the linewidth of the NO absorption transition at the low pressures commonly found within supersonic and hypersonic wind tunnels. Laser frequency scans using a pulsed laser system with high-spectral-resolution were performed by Kulatilaka *et al.* [9] and Naik *et al.* [10] using an optical parametric oscillator system for 2D imaging, i.e., *planar* laser induced fluorescence (PLIF). More recently, high-spectral-resolution 2D PLIF measurements have been performed at 1 kHz by Wang and Hanson [11] using a relatively high-power CW laser system.

We report high-spectral-resolution NO-PLIF measurements in the present work at a repetition rate of 100 kHz, which is 10,000 times greater than the high-spectral-resolution NO-PLIF measurements reported by Kulatilaka *et al.* [9] and Naik *et al.* [10]. The system uses a burst-mode laser [12] and an injection-seeded optical parametric oscillator for tunable, ultraviolet (UV) pulses at a high repetition rate. The laser frequency (i.e. wavelength) is rapidly scanned over two neighboring absorption transitions by varying the current of the 1064 nm seed laser used as the oscillator of the burst-mode laser system. Sufficiently narrow laser linewidth and small step size are essential to obtain information on the flow parameters (temperature, pressure, velocity) through a LIF excitation scan, as the spectral width of the tunable laser must be significantly smaller than the spectral width of the molecular resonance.

In the present work, we use the measured frequency shift for the spectral position of the peak LIF intensity to infer flow properties of pressure and velocity. As noted in references such as Eckbreth [13], the frequency shift of the absorption transition is due to contributions from the collisional shift and the Doppler shift. The empirically obtained coefficients and exponents to relate thermodynamic properties of temperature and pressure to the collisional shift depends on the composition of the gas mixture. References such as DiRosa *et al.* [14] provide the coefficients and exponents for small mole fractions of NO in N_2. For the present work, the following expression is used for the collisional shift:

$$\delta\nu_{\mathrm{C}} = -0.18\frac{P\,[kPa]}{101.32\,[kPa]}\left(\frac{300\,[K]}{T\,[K]}\right)^{0.56}. \tag{1}$$

The Doppler shift for the spectral position of the peak LIF intensity can be approximated as:

$$\delta\nu_{\mathrm{D}} = \frac{U}{c}\nu_0, \tag{2}$$

where U is the flow speed in the direction of propagation of the laser sheet, c is the speed of light, and ν_0 is the known absorption line position.

By scanning over two different absorption transitions, a two-line rotational thermometry approach is used to measure the gas temperature. The reader is referred to references such as Eckbreth [13] and Palma [15] for a more thorough background on LIF thermometry. The equation for the two-line NO-PLIF thermometry is based on:

$$\frac{S_{\mathrm{F},\alpha}}{S_{\mathrm{F},\beta}} = C\left(\frac{E_\alpha}{E_\beta}\right)\left(\frac{B_{12,\alpha}(2J+1)_\alpha}{B_{12,\beta}(2J+1)_\beta}\right)exp\left(\frac{-\left(\left(\frac{\Delta E}{k_B}\right)_\alpha-\left(\frac{\Delta E}{k_B}\right)_\beta\right)}{T}\right). \tag{3}$$

In the above equation, the subscripts α and β refer to two different absorption transitions, S_{F} is the fluorescence signal measured by the detector, E is the monitored laser energy, and C is a calibration constant. In the present work, $C = 1$ due to the reasons proposed by Palma [15], which include the use of the same camera and laser systems for both transitions and based on the common assumptions used for NO spectroscopy such as J and T independence. Spectroscopic parameters used for the two-line thermometry approach include the Einstein B coefficient B_{12}, the rotational quantum number of the ground state J, and the rotational energy of the transition $\Delta E/k_B$. While only two absorption transitions are used in this work due to limitations in the scan range that could be achieved within a single burst, the thermometry analysis is similar to the one adopted by Foo *et al.* [16], which has been made publicly available within the LIF program Thermo-NO-LIF.

II. Experimental Systems

A schematic diagram of the 100 kHz planar laser induced fluorescence system is shown in Fig. 1. The burst-mode laser and optical parametric oscillator (OPO) are very similar to the one previously described by Hsu *et al.* [17, 18] and only a brief description is provided here. In this work, the burst-mode laser was operated at a repetition rate

of 100 kHz for a burst duration of approximately 2.5 ms, yielding approximately 200 laser pulses at 226 nm. The burst length was limited to 2.5 ms, rather than the 10.5 ms burst commonly used with the burst-mode laser system, in order to reduce the risk of damaging optics within the OPO system. A CW seed laser near 1064 nm was used as the oscillator for the burst-mode laser with seven amplifier stages to provide high pulse energy even at a repetition rate of 100 kHz. Most of the third harmonic output near 355 nm from the burst-mode laser was used to pump the OPO, which was seeded with a CW laser at an OPO idler wavelength near 823 nm. The OPO signal generated near 623 nm was sum-frequency-mixed with the remaining 355 nm from the burst-mode laser to generate the 226-nm laser needed for NO-PLIF. The laser energy at 226 nm was as high as 1 mJ/pulse during the relatively constant laser energy portion of the burst and the full-width-at-half-maximum (FWHM) laser linewidth at 226 nm is believed to be approximately 0.015 cm^{-1}. The 226-nm laser energy was monitored using a photodiode and measured on an oscilloscope.

The fast frequency scans were performed by using a function generator at a frequency of 500 Hz to tune the current of the 1064 nm laser diode during the scan, which varied the laser frequency. Due to the non-linear optical processes used to convert the fundamental 1064 nm from the burst-mode laser to the 226 nm used for NO-PLIF, varying the 1064 nm laser resulted in a factor of 6 larger variation at 226 nm (e.g. a 0.001 cm^{-1} variation at 1064 nm resulted in a 0.006 cm^{-1} variation at 226 nm). The signal provided by the function generator to the 1064 nm seed laser was also measured by the same oscilloscope. The function generator was triggered in a manner that allowed a scan from higher wavenumbers to lower wavenumbers to occur over 100 laser shots (1 ms) during the relative constant laser energy portion of the 2.5 ms burst.

The 226 nm laser beam was directed to an underexpanded jet flow after being expanded into a laser sheet using a negative-75-mm-focal-length cylindrical lens and a positive-400-mm-focal-length spherical lens system. The underexpanded jet system featured a sonic nozzle with an exit diameter of approximately 2.6 mm and flowed a mixture of 300 ppm nitric oxide in nitrogen at ambient temperature. The jet stagnation pressure was measured upstream of the nozzle using a pressure transducer (GE Druck PACE1000). Two different jet stagnation pressure conditions are reported in this work, corresponding to approximately 0.5 MPa and 1 MPa. The jet flow exited to air at atmospheric pressure and therefore jet stagnation to ambient pressure ratios (P_0/P_a) of 5 and 10 are reported in this work. The direction of propagation for the laser sheet was orthogonal to the jet flow. PLIF images were captured using a Photron FASTCAM SA-Z camera equipped with a LaVision UV IRO and a 100 mm *f*/2.8 UV lens. Macro rings were used with the camera lens to enable a spatial resolution of approximately 26 μm/pix.

The laser frequency was scanned over two different neighboring NO transitions: the overlapping $R_1(5.5)$ + $Q_{21}(5.5)$ line pair near 44,223.9 cm^{-1} and the overlapping $Q_1(11.5)$ + $P_{21}(11.5)$ line pair near 44,221.9 cm^{-1}. These line pairs were chosen because: 1) their energy levels are separated enough so that their signal intensity ratio provides sufficient temperature sensitivity (while having energy levels close enough such that both line pairs yield high signal-to-noise ratio images for the flow field studied), and 2) the line positions of the two pairs are close enough such that both transitions can be excited during a single scan (while having line positions separated enough such that both line pairs can be resolved at moderate pressures). Figure 2 shows the simulated LIF excitation spectra using LIFBASE [19] for temperatures of 100 K and 300 K and at three different pressures corresponding to 1 kPa, 10 kPa, and 100 kPa. The temperature sensitivity of the $Q_1(11.5)$ + $P_{21}(11.5)$ line pair relative to the $R_1(5.5)$ + $Q_{21}(5.5)$ line pair is evident. The effect of the collisional shift and broadening is also evident when comparing the spectra relative to the three pressures chosen for this simulation. At the highest pressure of 10 kPa, the collisional shift due to the temperature effect is also clear. Pressures exceeding 500 kPa are expected for the test conditions considered here. Therefore, relatively widely spaced lines (2 cm^{-1}) were chosen so that the lines would not fully overlap even at such high pressures.

III. Results and Discussion

Visualizations of the underexpanded jet flow field at a repetition-rate of 100 kHz during the fast frequency scan are presented in this section at two different jet stagnation pressure ratios corresponding to $P_0/P_a = 5$ and $P_0/P_a = 10$. Single-shot PLIF images of the underexpanded jet at the $P_0/P_a = 5$ condition are shown in Fig. 3. Figure 3(a) shows the images acquired near the peak of the overlapping $R_1(5.5)$ + $Q_{21}(5.5)$ transition pair and Fig. 3(b) shows the images acquired near the peak of the overlapping $Q_1(11.5)$ + $P_{21}(11.5)$ transition pair. The $P_0/P_a = 5$ jet appears to be moderately underexpanded and the location of the first diamond shock can be inferred from the images. The jet appears to be relatively steady near the nozzle exit but the level of unsteadiness in the region downstream of the shock is such that the images do not appear to be correlated at 100 kHz.

Single-shot PLIF images of the underexpanded jet at the $P_0/P_a = 10$ condition are shown in Fig. 4. The $P_0/P_a = 10$ jet appears to exhibit features of a strongly underexpanded jet, including the barrel shock and the Mach disk. At the 100 kHz repetition-rate, the jet appears to be steady in the region upstream of the Mach disk. However, the

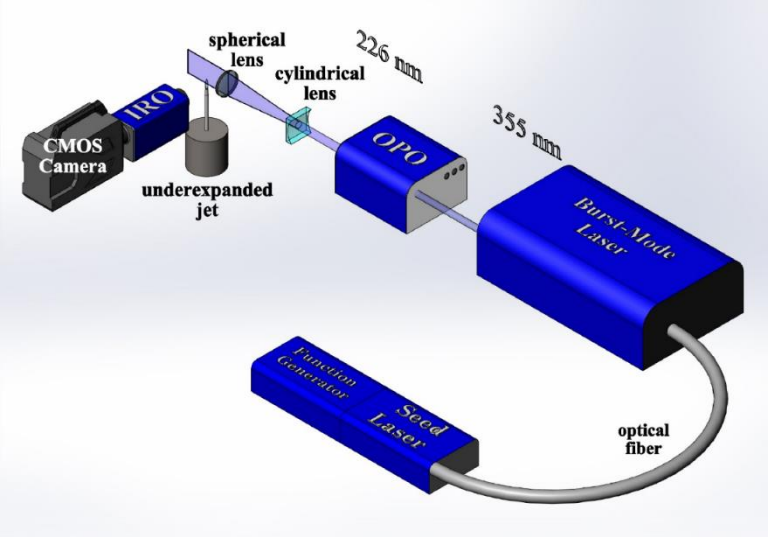

Figure 1. Schematic of the burst-mode laser and optical parametric oscillator (OPO) system used for the fast frequency scan with the underexpanded jet and high-speed intensified camera system.

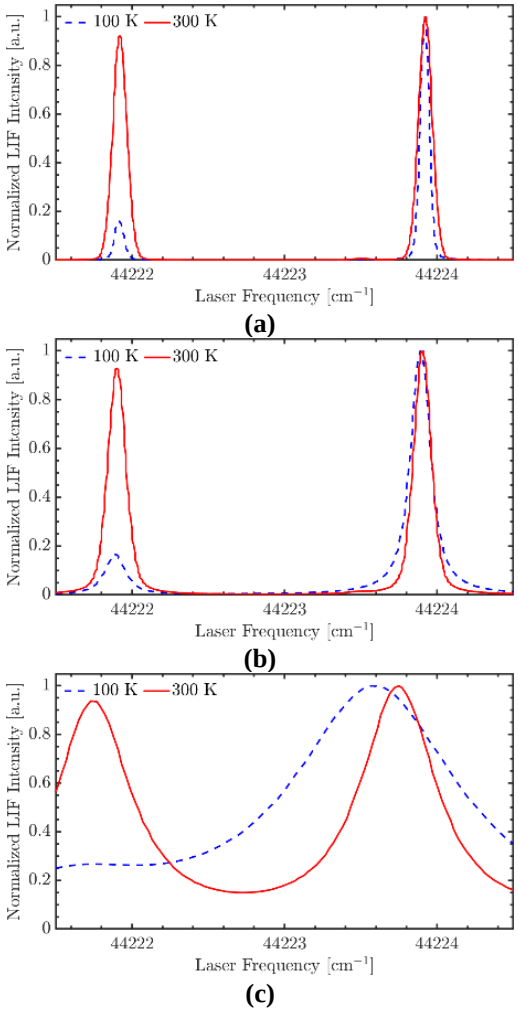

Figure 2. Simulated normalized LIF intensity vs. laser frequency using LIFBASE at 100 K and 300 K for three different pressures corresponding to (a) 1 kPa, (b) 10 kPa, and (c) 100 kPa.

unsteadiness in the region downstream of the Mach disk and within the shear layers do not appear to be correlated for the images acquired at 100 kHz. As the laser frequency is scanned for both of the transition pairs (scanned from higher to lower wavenumbers), the PLIF signal distribution appears to vary along the axial (z) direction of the underexpanded jet. The sensitivity of the PLIF signal along this direction (e.g. the jet centerline) is due to the collisional shift induced by the flow and could only be revealed with such a narrow-linewidth laser. This shows the potential for high-speed, high-spectral-resolution PLIF measurements using the burst-mode laser with a seeded optical parametric oscillator. Furthermore, since the direction of laser sheet propagation is perpendicular to the jet flow, it appears that the Doppler shift is relatively small when comparing the radial distribution of the PLIF signal as the left-side ($r < 0$) and right-side ($r > 0$) of the jet appear to be similar.

The next two sub-sections show results for the $P_0/P_a = 10$ condition only, with the focus on fitting the LIF spectra at each pixel to measure the frequency shift and amplitude. We use the axisymmetric nature of the flow field to separate the measured frequency shift into collisional and Doppler components and use the amplitude of the measured peaks for two-line thermometry, with the motivation of multi-parameter measurements of temperature, pressure and one component of velocity.

A. Pseudo-Voigt fitting of LIF excitation spectra

The LIF excitation spectra at each pixel was fitted using a pseudo-Voigt line shape function similar to the approach in the program Thermo-NO-LIF [16]. The pseudo-Voigt line shape function used herein is a linear combination (rather than convolution) of the Gaussian and Lorentzian functions and does not explicitly consider the spectroscopic parameters. Two different forms of the pseudo-Voigt equation were formatted depending on whether the fit was performed for only one transition pair (the overlapping $R_1(5.5) + Q_{21}(5.5)$ pair) or for both transition pairs (both the overlapping $R_1(5.5) + Q_{21}(5.5)$ pair and the overlapping $Q_1(11.5) + P_{21}(11.5)$ pair).

The equation used for fitting only the $R_1(5.5) + Q_{21}(5.5)$ pair was:

$$V(A,B,\Gamma,\eta,\hat{\nu},\nu) = A\left\{(1-\eta)exp\left[-4ln(2)\left(\frac{\nu-\hat{\nu}}{\Gamma}\right)^2\right] + (\eta)\left[1+4\left(\frac{\nu-\hat{\nu}}{\Gamma}\right)^2\right]^{-1}\right\} + B. \quad (4)$$

In the above equation: V is the pseudo-Voigt line shape function, whereas A and B are the amplitude and baseline, respectively. V, A, and B have the same arbitrary unit of LIF intensity, which is shown here as [a.u.]. Γ and $\hat{\nu}$ are the full-width-at-half-maximum (FWHM) linewidth and spectral position of the peak intensity, respectively, and both possess the wavenumber unit [cm^{-1}]. The dimensionless weighting parameter for the linear combination is η. The five parameters $A, B, \Gamma, \eta, \hat{\nu}$ are obtained through fitting of the amplitude of the signal as a function of wavenumber ν [cm^{-1}], which is the independent variable in the equation. Fitting only the $R_1(5.5) + Q_{21}(5.5)$ pair allows for the extraction of the observed frequency shift using the equation,

$$\delta\nu = \hat{\nu} - \nu_0, \quad (5)$$

where ν_0 is the known line position from LIFBASE [19] without considering any collisional shift or Doppler shift effects. The observed frequency shift may be due to contributions from both collisional shift and Doppler shift.

The pseudo-Voigt equation used for fitting both the $R_1(5.5) + Q_{21}(5.5)$ pair and the $Q_1(11.5) + P_{21}(11.5)$ pair was:

$$\begin{aligned} V(A_\alpha, A_\beta, B, \Gamma, \eta, \hat{\nu}_\alpha, \hat{\nu}_\beta, \nu) = {} & A_\alpha\left\{(1-\eta)exp\left[-4ln(2)\left(\frac{\nu-\hat{\nu}_\alpha}{\Gamma}\right)^2\right] + (\eta)\left[1+4\left(\frac{\nu-\hat{\nu}_\alpha}{\Gamma}\right)^2\right]^{-1}\right\} \\ & + A_\beta\left\{(1-\eta)exp\left[-4ln(2)\left(\frac{\nu-\hat{\nu}_\beta}{\Gamma}\right)^2\right] + (\eta)\left[1+4\left(\frac{\nu-\hat{\nu}_\beta}{\Gamma}\right)^2\right]^{-1}\right\} + B \end{aligned} \quad (6)$$

The parameters in Eq. 6 are similar to those in Eq. 4, with the use of subscripts to distinguish the amplitude (A_α and A_β) and peak spectral position of the LIF intensity ($\hat{\nu}_\alpha$ and $\hat{\nu}_\beta$) for the two transition pairs. The fit produces a single value for the baseline, FWHM linewidth, and weighting parameter for the linear combination, as these are solely dependent on the linewidth of the laser and the thermodynamic properties of the gas and are not dependent on the transition pair probed.

Selected 2D PLIF images of the underexpanded jet at the $P_0/P_a = 10$ condition during the fast frequency scan are shown in Fig. 5(a). The images, which correspond to the estimated laser frequencies shown in Fig. 5(b), show the underexpanded jet at: (1) the peak of the $R_1(5.5) + Q_{21}(5.5)$ transition pair, (2) several detuned (lower) wavenumbers

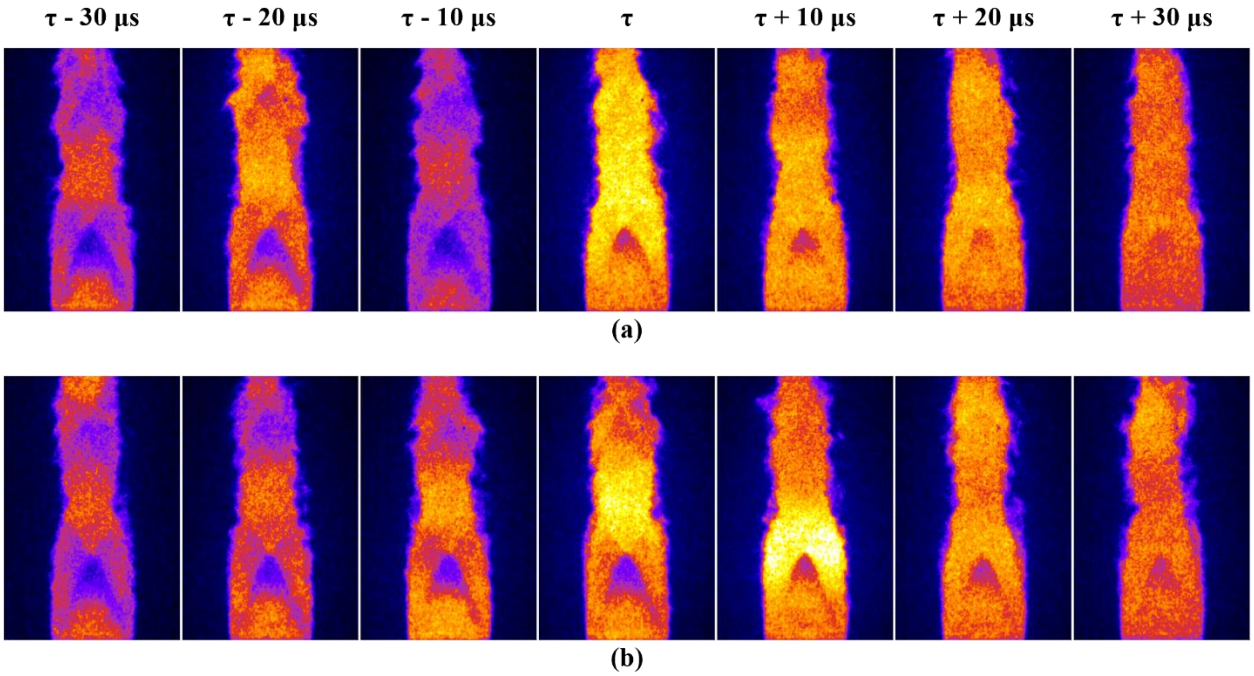

Figure 3. Sequence of 100 kHz PLIF images of the P_0/P_a = 5 underexpanded jet during a frequency scan near: (a) the overlapping $R_1(5.5)$ + $Q_{21}(5.5)$ transition pair and (b) the overlapping $Q_1(11.5)$ + $P_{21}(11.5)$ transition pairs. Both pairs are covered over the scan duration of 1 ms during a single burst, with the scan occurring from higher to lower laser frequencies.

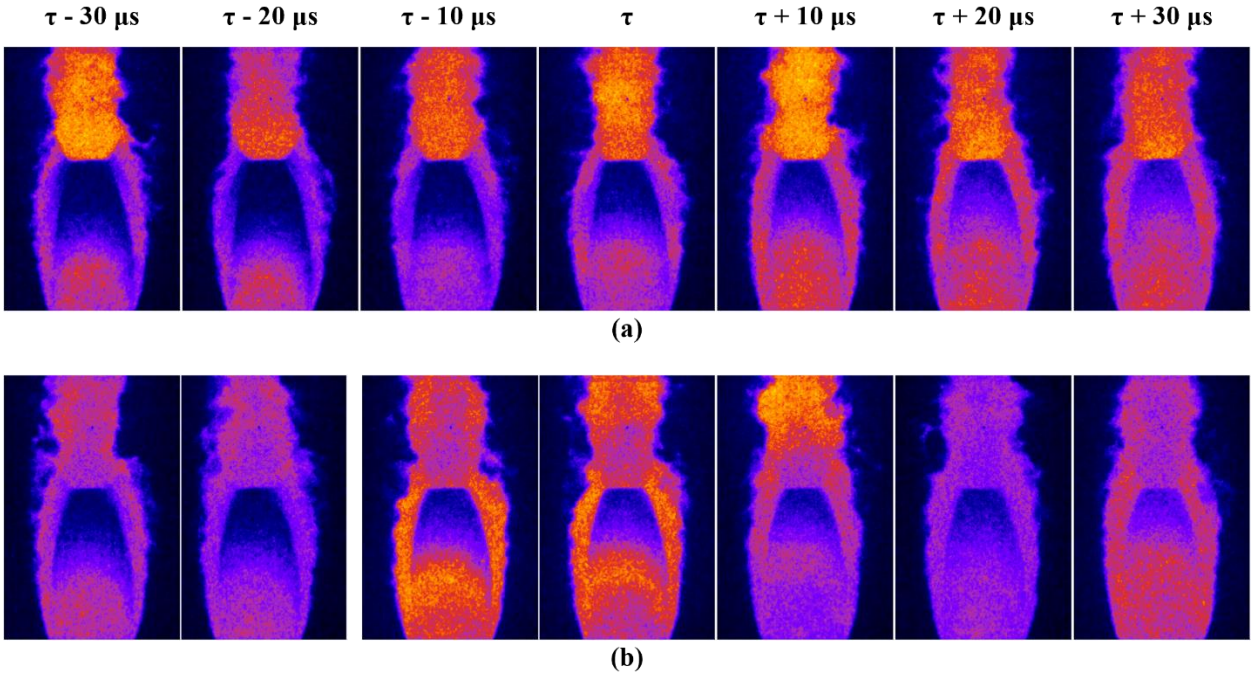

Figure 4. Sequence of 100 kHz PLIF images of the P_0/P_a = 10 underexpanded jet during a frequency scan, from higher to lower laser wavenumbers, near: (a) the overlapping $R_1(5.5)$ + $Q_{21}(5.5)$ transition pair and (b) the overlapping $Q_1(11.5)$ + $P_{21}(11.5)$ transition pairs. Both pairs are covered over the scan duration of 1 ms during a single burst, with the scan occurring from higher to lower laser frequencies.

from the peak of this line pair, (3) several detuned (higher) wavenumbers from the peak of the $Q_1(11.5) + P_{21}(11.5)$ transition pair, and (4) the peak of this line pair. Figures 5(b) and 5(c) show the LIF intensity vs. estimated laser frequency at two different spatial locations along the jet centerline. The locations correspond to a relatively low-pressure, low-temperature region upstream of the Mach disk (r = 0 mm, z = 4.5 mm) and a relatively high-pressure, high-temperature region downstream of the Mach disk (r = 0 mm, z = 5.0 mm). At both of these locations, pseudo-Voigt fits using only the $R_1(5.5) + Q_{21}(5.5)$ transition pair are shown with the solid red line and fits using both the $R_1(5.5) + Q_{21}(5.5)$ and $Q_1(11.5) + P_{21}(11.5)$ transition pairs are shown in dashed blue.

Examining the LIF excitation spectra in Fig. 5(b) and Fig. 5(c) show some significant levels of scatter in the data. This can be attributed to: (1) fluctuations in the shot-to-shot energy distribution of the laser sheet, and (2) uncertainty in the actual laser frequency during the scan. Several approaches were investigated to correct for the shot-to-shot energy distribution of the laser sheet, including using a beam splitter to reflect ~1% of the laser energy to a BK7 glass diffuser plate and capturing the non-intensified blue fluorescence with a 2nd high-speed CMOS camera. However, the lifetime of the fluorescence from the glass diffuser plate was determined to be long enough such that signal from the preceding laser pulse was also captured. A second approach to measure the bulk laser energy fluctuation using a beam splitter before the sheet forming optics and reflecting ~1% of the laser energy to a UVFS ground glass diffuser was also explored. Although the lifetime of the fluorescence from the UVFS ground glass diffuser was determined to be suitable for the current application at 100 kHz, applying the bulk laser energy correction to the 2D images did not improve the measurement quality. This suggests the presence of shot-to-shot variations in the energy distribution of the laser sheet during the burst, rather than simply variations in the bulk laser energy. The results shown in this paper do not correct for the shot-to-shot variations in the energy distribution of the laser. This may be less significant for low-pressure regions such as the r = 4.5 mm, z = 0 mm location shown in Fig. 5(b), where full or partial saturation of the LIF transition reduces the impact that laser energy variations has on the laser-induced fluorescence. However, it is expected that correcting for the shot-to-shot variations in the energy distribution of the laser will improve the data quality for higher pressure regions such as the r = 5.0 mm, z = 0 mm location.

Several approaches were also investigated to reduce the uncertainty of the actual laser frequency during the fast frequency scan. One such approach involved splitting the output from the function generator to the 1064 nm seed laser and measuring the voltage on an oscilloscope during the scan. Although this approach may have satisfactorily measured the voltage going into the seed laser, it did not measure the response of the seed laser and therefore did not significantly help with correcting the laser frequency axis. A low-speed wavemeter was used to measure the 1064 nm seed laser at either ends of the scan range. However, comparing the calculated frequency step size from this approach to the estimated frequency step size based on the known line positions of the LIF transitions used in this work showed significant differences. Therefore, the results in this paper use the peak LIF intensity within the lowest pressure region upstream of the Mach disk (estimated to be ~10 kPa and ~100 K based on Ref. 20) to anchor the scan to the known 2.0 cm^{-1} spacing in line positions of the $R_1(5.5) + Q_{21}(5.5)$ and $Q_1(11.5) + P_{21}(11.5)$ transition pair. The frequency step size is estimated based on the number of images in between the two peaks and is reported here to be approximately 0.020 cm^{-1}. Based on the collisional shift at 10 kPa and 100 K, we estimate the error in the absolute line position to be approximately 0.030 cm^{-1}. It is noted that the error in the absolute line position is insignificant when determining the frequency shift, but the error in the relative line position (caused by potentially varying step size during the scan) is critically important.

Although we expect higher than desired levels of uncertainty in this data due to variations in the laser sheet energy distribution and uncertainty in the laser frequency during the scan, the qualitative nature of the high-spectral-resolution measurements are clear. The spectral positions of the peak intensity show a clear shift when comparing the relatively low-pressure region of the flow before the Mach disk in Fig. 5(b) and the relatively high-pressure region of the flow after the Mach disk in Fig. 5(b). The observed frequency shift is especially clear when comparing the one-dimensional LIF excitation spectra of the underexpanded jet. Figure 6(a) and 6(b) show the 1D LIF excitation spectra before the Mach disk (axial location fixed at z = 4.5 mm) and after the Mach disk (axial location fixed at z = 5.0 mm) and Fig. 6(c) shows the 1D LIF excitation spectra along the jet centerline (radial location fixed at r = 0). Also shown here are the centroids from pseudo-Voigt fits obtained by fitting only the overlapping $R_1(5.5) + Q_{21}(5.5)$ pair (solid red) and fitting both the $R_1(5.5) + Q_{21}(5.5)$ pair and the $Q_1(11.5) + P_{21}(11.5)$ pair (open blue). The physical locations of the 1D lines relative to the 2D PLIF image are in Fig. 6(d), which shows a 2D PLIF image of the underexpanded jet averaged over the 1 ms scan.

The frequency shift due to collisional shift only can be seen in Fig. 6(c), which shows the 1D LIF excitation spectra at the jet centerline. For the $R_1(5.5) + Q_{21}(5.5)$ transition near 44223.9 cm^{-1}, the frequency shift towards lower

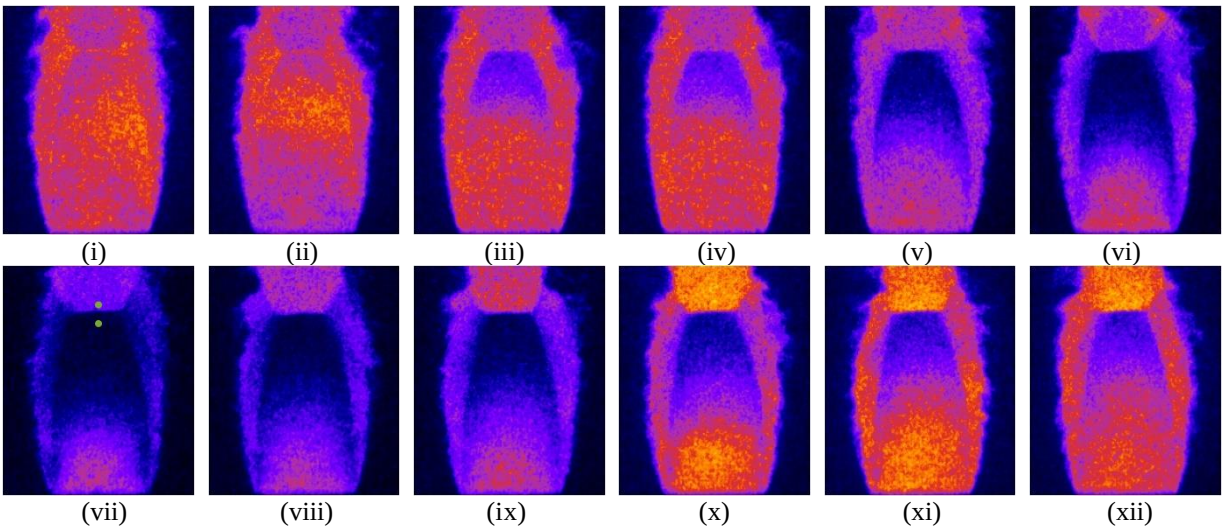

(a)

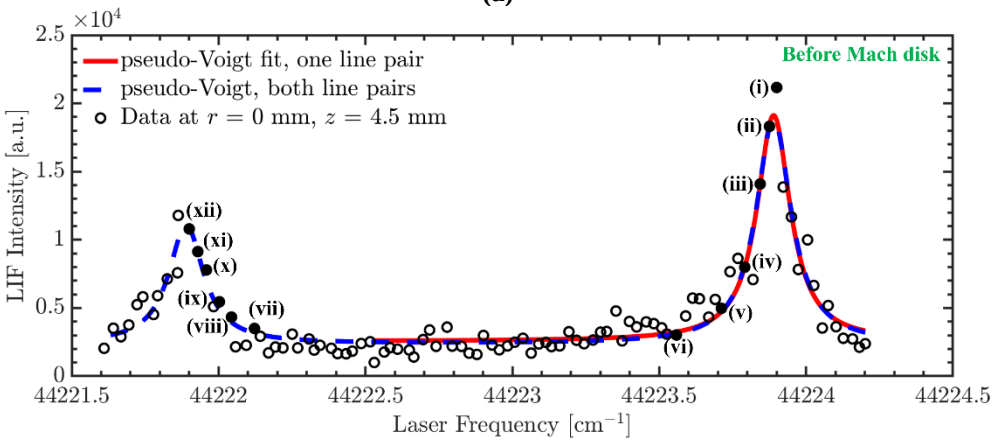

(b)

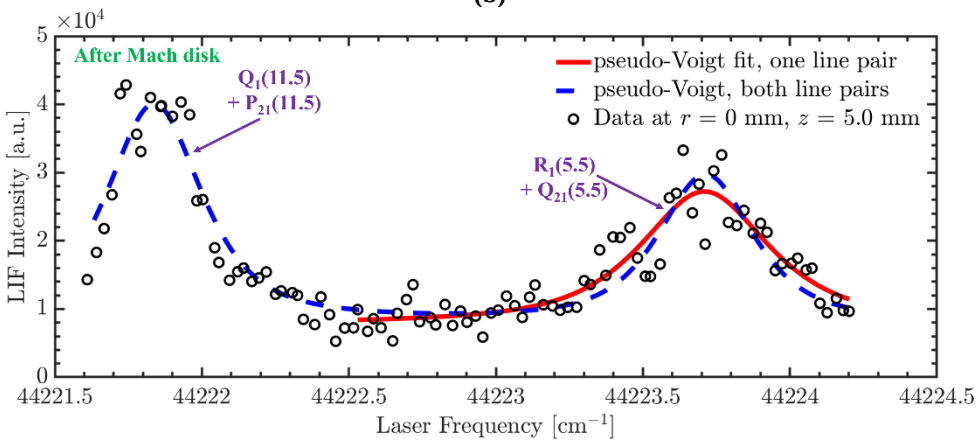

(c)

Figure 5. (a) Select 2D PLIF images during the fast frequency scan, which was performed at 100 kHz from higher wavenumbers to lower wavenumbers over a time period of 1 ms. The LIF intensity vs. laser frequency (wavenumber) at the centerline (*r* = 0 mm) of the underexpanded jet is shown at a location: (b) upstream of the Mach disk at *z* = 4.5 mm and (c) downstream of the Mach disk at *z* = 5.0 mm. The PLIF images in (a) correspond to the laser frequencies indicated in (b). Image *vii* in 5(a) also indicates the spatial location for the LIF spectra shown in 5(b) and 5(c). Also shown in 5(b) and 5(c) are pseudo-Voigt fits obtained from fitting only the overlapping $R_1(5.5) + Q_{21}(5.5)$ transition (solid red) and fitting both the $R_1(5.5) + Q_{21}(5.5)$ transition and the $Q_1(11.5) + P_{21}(11.5)$ transition (dashed blue).

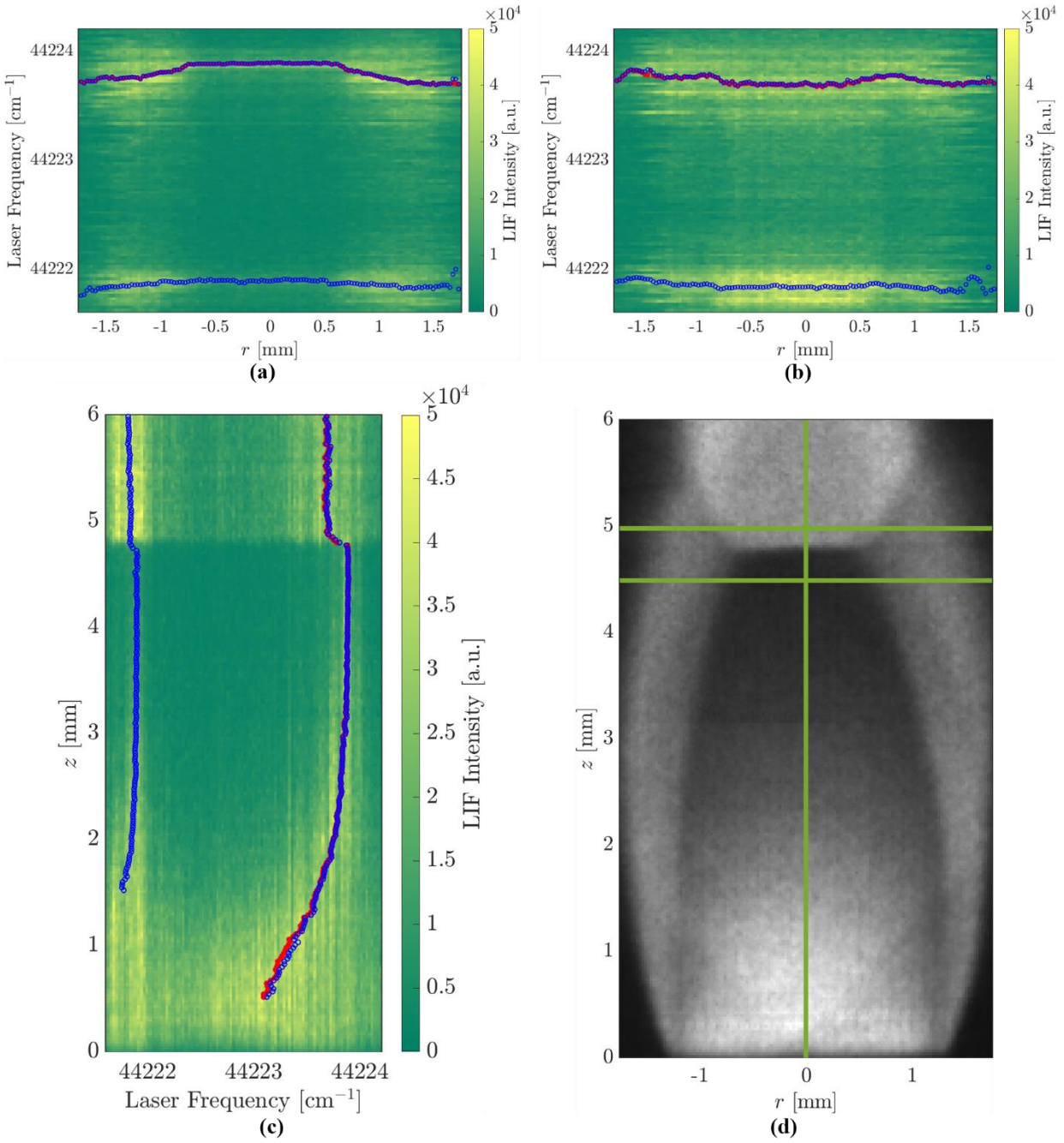

Figure 6. 1D LIF excitation spectra extracted from the 2D PLIF images illustrating the frequency (wavenumber) shift: (a) upstream of the Mach disk at *z* = 4.5 mm, (b) downstream of the Mach disk at *z* = 5.0 mm, and (c) along the centerline (*r* = 0) of the underexpanded jet, (b) before. Also shown are the centroids from pseudo-Voigt fits obtained by fitting only the overlapping $R_1(5.5) + Q_{21}(5.5)$ pair near 44223.9 cm-1 (solid red) and fitting both the $R_1(5.5) + Q_{21}(5.5)$ pair and the $Q_1(11.5) + P_{21}(11.5)$ pair near 44221.9 cm-1 (open blue). An average 2D PLIF image over the over the fast frequency scan (100 shots at 100 kHz) is shown in (d) with the measurement locations for the 1D excitation spectra shown delineated in green.

wavenumbers is evident for relatively high-pressure regions closer to the jet exit. In addition, the discontinuity over the Mach disk is also clearly evident, with the sharp frequency shift towards lower wavenumbers observed for the relatively high-pressure region immediately after the Mach disk. Although the same qualitative behavior is observed for the $Q_1(11.5) + P_{21}(11.5)$ pair near 44221.9 cm^{-1}, the magnitude of the shift appears to be quite different. We believe that this is due to the apparent non-linear behavior of the seed laser near the end of the scan (the laser is scanned from higher wavenumbers to lower wavenumbers), which results in varying step size for the laser frequency. Furthermore, the centroids shown from the pseudo-Voigt fits, and the resulting frequency shifts, shown are limited to z = 1.5 mm in Fig. 6(c), since the even higher-pressure regions near the jet exit push the spectral positions of the peak intensity beyond the current scan range.

The frequency shifts seen in Fig. 6(a) and 6(b) contain both the collisional shift and the Doppler shift. Evidence of the Doppler shift can be seen with the centroids from the pseudo-Voigt fits for the left side (r < 0 mm) appearing to be at a lower wavenumber than the right side (r > 0 mm). Evidence of the collisional shift can be seen in Fig. 6(a), with the centroids from the pseudo-Voigt fits for the relatively lower pressure region in the jet core upstream of the Mach disk being at higher wavenumbers than the relatively higher-pressure regions outside of the jet core. The inverse effect can be seen in Fig 6(b), with the relatively higher-pressure regions downstream of the Mach disk having centroids from the pseudo-Voigt fits at greater wavenumbers than the relatively lower pressure regions within the slipstream.

B. Towards temperature, pressure, and velocity measurements

Using the spectral positions of the peak intensity based on the pseudo-Voigt fits from only the overlapping $R_1(5.5) + Q_{21}(5.5)$ transition and the known line position from LIFBASE, the 2D frequency shift image was computed. This is shown in Fig. 7(a) for the P_0/P_a = 10 jet at locations of the image within the jet boundary, which was determined based on an edge-detection algorithm. While the 2D frequency shift image along the jet centerline is due only to collisional shift effects, since the direction of propagation for the laser sheet is normal to the axisymmetric jet flow, all other regions of the flow have some frequency shift contributions from the Doppler shift. Using the axisymmetric assumption for the jet flow, the frequency shift was separated into the collisional shift ($\delta\nu_C$) shown in Fig. 7(b) and the Doppler shift ($\delta\nu_D$) shown in Fig. 7(c). As expected, the largest collisional shift is observed near the nozzle exit and a negligible collisional shift is observed at the relatively low-pressure region immediately upstream of the Mach disk. A sharp increase in the collisional shift can also be seen in the region immediately downstream of the Mach disk. While the Doppler shift contribution is relatively low within most of Fig. 7(c), the region of the flow field that corresponds to expansion fans and oblique shocks show the largest Doppler shift.

Although the images shown in Fig. 7 are shown quantitatively with units of [cm^{-1}], we expect significant uncertainty in the measurement due to the estimation of the laser wavelength during the fast frequency scan. In future efforts, we plan to monitor one or more of the following wavelengths during the frequency scan using a Fabry-Pérot etalon: (1) residual 1064 nm or 532 nm from the burst-mode laser, (2) residual 624 nm or 355 nm from the OPO, or (3) using a beam splitter to pick-off ~1% of the 226 nm laser. A high-speed wavemeter could also be used as an alternative to the Fabry-Pérot etalon.

The rotational temperature of the flow is calculated by the two-line thermometry method, where in this work the ratio of the amplitude from the pseudo-Voigt fits are used to calculate temperature. Figure 8(a) shows the computed 2D amplitude of the LIF intensity from pseudo-Voigt fits obtained by fitting the overlapping $R_1(5.5) + Q_{21}(5.5)$ transition pair and Fig 8(b) shows the 2D amplitude obtained by fitting the overlapping $Q_1(11.5) + P_{21}(11.5)$ transition pair. The ratio of the 2D amplitudes $[(Q_1(11.5) + P_{21}(11.5)) / (R_1(5.5) + Q_{21}(5.5))]$ is shown in Fig 8(c). While the 2D ratio image in Fig 8(c) shows the expected trend for temperature (e.g. lower values for the ratio upstream of the Mach disk compared to downstream), we believe that the temperature measurement is complicated because of the following reasons: (1) scatter in the LIF spectra, especially within the relatively high-pressures regions of the flow, due to variations in the shot-to-shot energy distribution of the laser sheet not accounted for, (2) potential laser absorption effects, particularly in the relatively high-pressure region of the flow, due to the strongly absorbing $Q_1(11.5) + P_{21}(11.5)$ transition pair used, and (3) potential complications caused by partial-saturation of the LIF transition, especially within the relatively low-pressure region of the flow, due to differing values of the Einstein B coefficient (B_{12}) for the two line pairs.

Nevertheless, a 2D gas temperature measurement was attempted using the two-line Boltzmann method, which has been recast from Eq. 3 to the following equation:

$$T = \frac{-1}{\frac{\log\left(\frac{A_\beta}{(2J+1)(B_{12})}\right)_\beta - \log\left(\frac{A_\alpha}{(2J+1)(B_{12})}\right)_\alpha}{\left(\frac{\Delta E}{k_B}\right)_\beta - \left(\frac{\Delta E}{k_B}\right)_\alpha}}. \tag{7}$$

In the above equation, the subscript α refers to the $R_1(5.5) + Q_{21}(5.5)$ line pair and β refers to the $Q_1(11.5) + P_{21}(11.5)$ line pair, J is the rotational quantum number of the ground state, and $\Delta E/k_B$ refers to the rotational energy of the line pair. Numerical values for A_α and A_β were determined on a pixel-by-pixel basis using the pseudo-Voigt fits. The numerical values for the spectroscopic quantities were obtained from Thermo-NO-LIF [16] and are shown in Table 1.

Using the measured collisional shift ($\delta\nu_C$) and temperature, the gas pressure can be calculated by recasting Eq. 1 to the following equation:

$$P\,[kPa] = (101.32\,[kPa]\,)\frac{\left(\frac{\delta\nu_C\,[cm^{-1}]}{-0.18\,[cm^{-1}]}\right)}{\left(\frac{300\,[K]}{T\,[K]}\right)^{0.56}}. \tag{8}$$

Based on this equation, it is clear that the accuracy of the pressure measurement is linearly related to the accuracy of the collisional shift measurement but is less sensitive to the accuracy of the temperature measurement due to the approximately square root dependence on temperature. Using the measured Doppler shift ($\delta\nu_D$), the radial velocity of the jet can be calculated by recasting Eq. 2 to the following equation:

$$V = (c\,)\frac{\delta\nu_D}{\nu_0}. \tag{9}$$

In the above equation, c is the speed of light and ν_0 is the known zero-velocity line position. Based on this equation, it is also clear that the accuracy of the velocity measurement is linearly related to the accuracy of the Doppler shift. Therefore, an accurate measurement of the laser frequency during the fast frequency scan is critically important to calculate gas velocity using this method.

The 2D temperature field for the underexpanded jet is qualitatively shown in Fig. 9(a). Assuming axisymmetric flow, which separated the frequency shift to the collisional shift and Doppler shift components, the measured pressure is qualitatively shown in Fig. 9(b) and the measured radial velocity is qualitatively shown in Fig. 9(c).

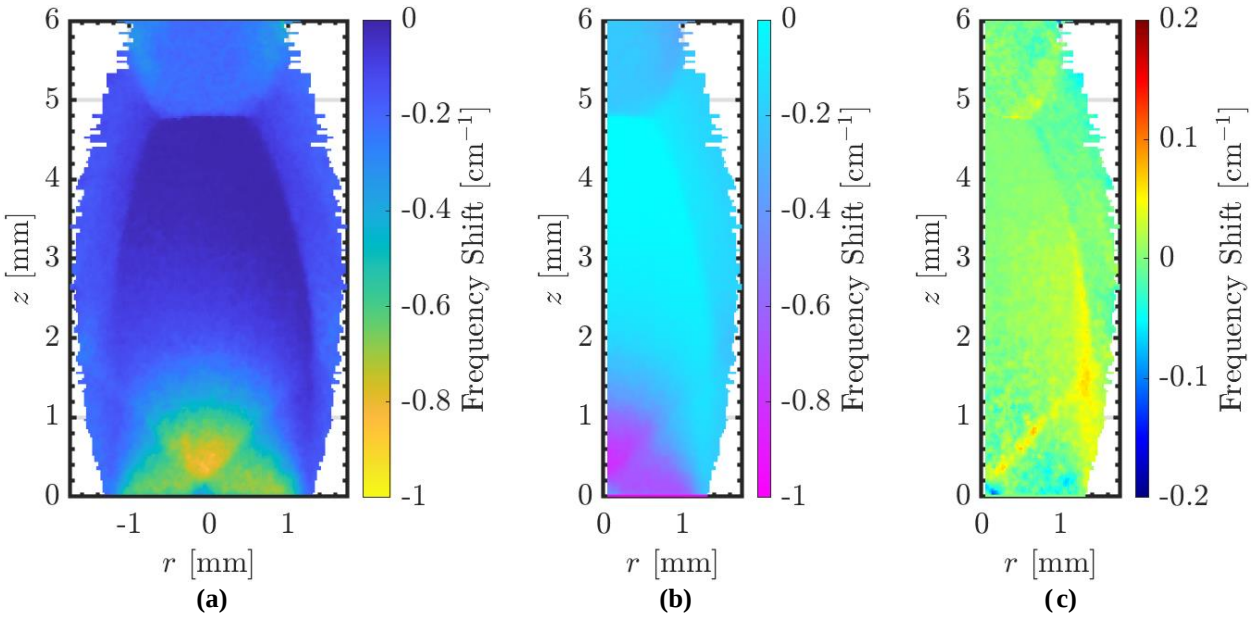

Fig. 7 (a) Computed 2D frequency shifts using centroids from pseudo-Voigt fits obtained by fitting the overlapping $R_1(5.5) + Q_{21}(5.5)$ transition only. The axisymmetric assumption was applied to the 2D frequency shift image to separate the (b) collisional shift and (c) Doppler shift.

Table 1. Spectroscopic properties of the two pairs of transitions from Thermo-NO-LIF [16].

		[-]	[-]	[K]
Line Pair	**Subscript**	$(2J+1)$	(B_{12})	$\Delta E/k_B$
$R_1(5.5) + Q_{21}(5.5)$	α	12	$8.357 \cdot 10^8$	$1.4516 \cdot 10^3$
$Q_1(11.5) + R_{21}(11.5)$	β	24	$9.357 \cdot 10^{10}$	$1.7114 \cdot 10^3$

IV. Summary and Conclusions

In the present work, we perform high-spectral resolution scanning NO-PLIF measurements of an underexpanded jet at a repetition-rate of 100 kHz using a burst-mode laser and optical parametric oscillator system. The laser frequency (wavelength) was varied over the burst to cover two neighboring absorption transition pairs by tuning the current of the 1064 nm seed laser of the burst-model laser using a function generator. As the laser frequency is scanned over the transition pairs (scanned from higher to lower wavenumbers), the PLIF signal distribution appears to vary along the axial (z) direction of the underexpanded jet. The sensitivity of the PLIF signal along this direction (e.g., the jet centerline) is due to the collisional shift induced by the flow and could only be revealed with such a narrow-linewidth laser. For the P_0/P_a = 10 condition we apply a pseudo-Voight fit to the LIF excitation spectra on a pixel-by-pixel basis to measure the spectral position of the peak intensity for the two transition pairs and their amplitude. The spectral position of the peak intensity and the known line position are used to measure the frequency shift, which is separated to its collisional and Doppler components using the axisymmetric nature of the flow field. The amplitude of the measured peaks is used for qualitative two-line rotational thermometry. Challenges for quantitative measurements using such an approach include the scatter in the LIF spectra due to fluctuations in the distribution of the laser sheet energy during the scan and an uncertainty in the step size of the frequency scan. For future efforts, we plan to simultaneously measure the laser energy distribution and the laser wavelength during the scan with the motivation of multi-parameter measurements of temperature, pressure, and velocity.

Acknowledgments

NSR and PMD acknowledge the support of the NASA Space Technology Mission Directorate (STMD) Game Changing Development (GCD) projects *Plume Surface Interaction and Entry Systems Modeling*, the NASA Exploration Systems Development Mission Directorate (ESDMD) project *Plume Surface Interaction*, and the NASA Aeronautics Research Mission Directorate (ARMD) Transformative Aeronautics Concepts Program (TACP) project *Transformational Tools and Technologies* (TTT). Funding for NSR during the initial part of this work was provided through an appointment to the NASA Postdoctoral Program at the NASA Langley Research Center, administered by

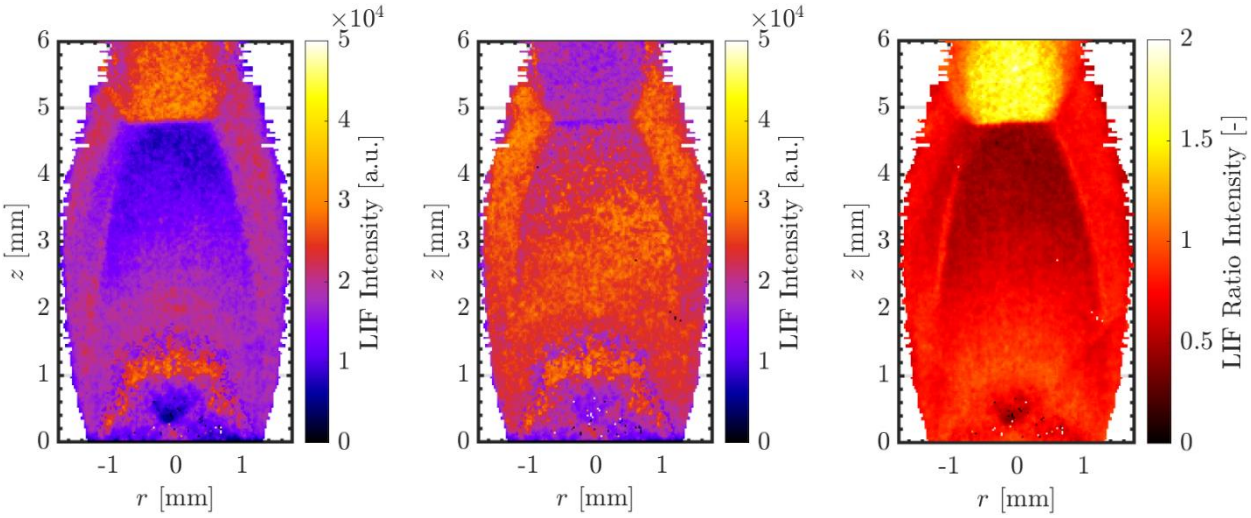

Fig. 8 Computed 2D amplitude of the LIF intensity from pseudo-Voigt fits obtained by fitting: (a) the overlapping $Q_1(11.5) + P_{21}(11.5)$ transition and (b) the overlapping $R_1(5.5) + Q_{21}(5.5)$ transition. The ratio $[(Q_1(11.5) + P_{21}(11.5)) / (R_1(5.5) + Q_{21}(5.5))]$ of the 2D amplitudes are shown in (c).

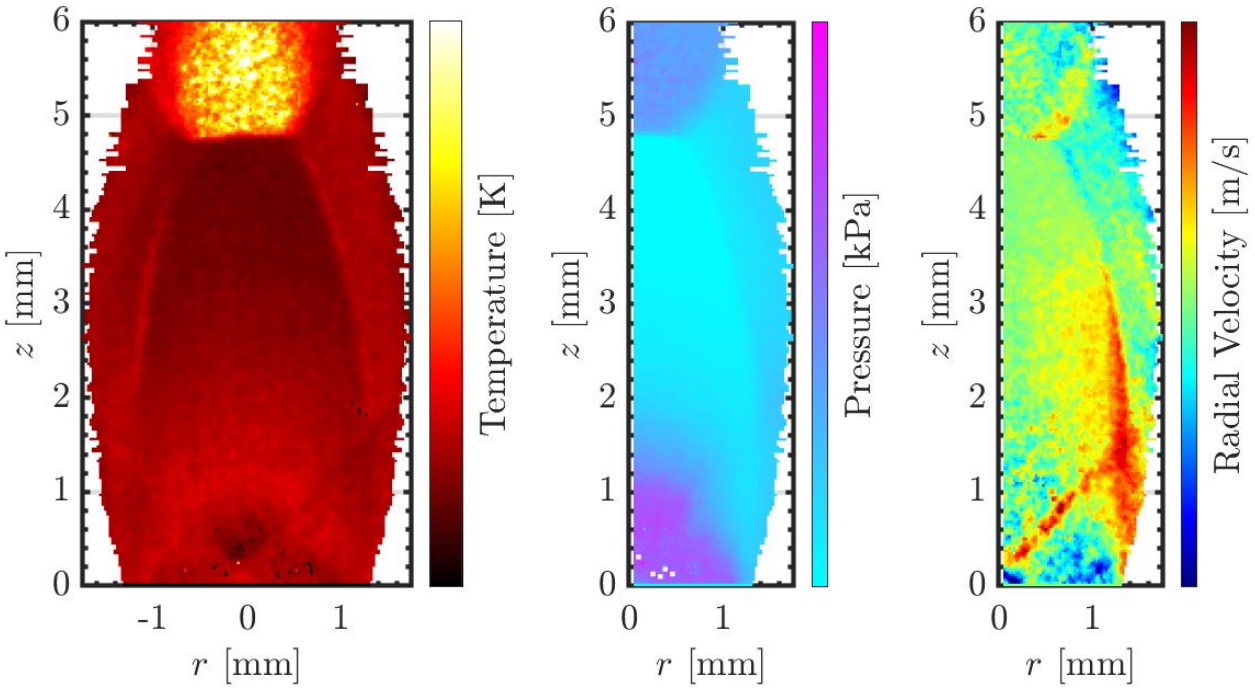

Figure 9. (a) 2D temperature field using the computed 2D amplitude of LIF intensity from pseudo-Voigt fits with the two-line thermometry method. The 2D temperature field was averaged at corresponding radial locations based on the axisymmetric nature of the flow and used with the 2D collisional shift from Fig. 7(b) to generate the 2D pressure field shown in (b). The 2D Doppler shift from Fig. 7(c) was used to generate the 2D radial velocity shown in (c).

Universities Space Research Association and later by Oak Ridge Associated Universities (ORAU) under contract with NASA. Funding for Spectral Energies (NJ, PH, JL, SR) to perform this work was granted by the STMD through a Phase II Small Business Innovation Research (SBIR) award under Contract No. 80NSSC20C0099. The authors thank Dr. Mikhail Slipchenko from Spectral Energies for his technical support with the burst-mode laser system and Andrew Kolonay from Spectral Energies for assistance with the build-up of the underexpanded jet system.

References

[1] Danehy, P. M., Weisberger, J., Johansen C., Resse, D., Fahringer, T., Parziale, N. J., Dedic C., Estevadeordal, J., Cruden, B. A., "Non-Intrusive Measurement Techniques for Flow Characterization of Hypersonic Wind Tunnels," NATO STO Manuscript on Hypersonic Freestream Characterization, 2018.

[2] Jiang, N., Hsu, P. S., Slipchenko, M., Roy, S., Lauriola, D. K., Webb, A. M., Meyer T. R., Gragston, M., Parker, R., Portoni, P., McDermott, C., Seitz, K., Wadhams, T. P., "MHz Rate Flow Diagnostics in the CUBRC Mach 10 Shock Tunnel," *AIAA Journal*, AIAA SciTech Forum, January 2022. doi: 10.2514/6.2022-1655.

[3] Drozda, T. G., Ground, C. R., Ziltz, A. R., Cabell K. F., Inman, J. A., Bathel, B. F., and Danehy, P. M., "Comparisons Between NO PLIF Imaging and CFD Simulations of Mixing Flowfields for High-Speed Fuel Injectors," 53rd AIAA/SAE/ASEE Joint Propulsion Conference, July 2017. doi: 10.2514/6.2017-4647.

[4] Rodrigues, N. S., Bathel, B. F., Danehy P. M., "A comparison of NO laser-induced fluorescence models at conditions relevant to supersonic and hypersonic flows," AIAA SciTech Forum, January 2022. doi: 10.2514/6.2022-0897.

[5] Zimmermann, M., Miles, R. B., "Hypersonic-Helium-Flow-Field Measurements with the Resonant Doppler Velocimeter," Applied Physics Letters, Vol. 37, No. 10, 1980, pp. 885–887. doi:10.1063/1.91784.

[6] McDaniel, J. C., Hiller, B., and Hanson, R. K., "Simultaneous Multiple Point Velocity Measurements Using Laser-Induced Iodine Fluorescence," *Optics Letters*, Vol. 8, No. 1, 1983, pp. 51–53.

[7] Di Rosa, M. D., Chang, A. Y., Hanson, R. K., "Continuous wave dye-laser technique for simultaneous, spatially resolved measurements of temperature, pressure, and velocity of NO in an underexpanded free jet," *Applied Optics*, Vol. 32, No. 21, 1993, pp. 4074–4087.

[8] Danehy, P. M., Mere, P., Gaston, J., O'Byrne, S., Palma, P. C., Houwing, A. F. P., "Fluorescence Velocimetry of the Hypersonic, Separated Flow over a Cone," *AIAA Journal*, Vol. 39, No. 7, 2001, pp. 1320-1328. doi: 10.2514/2.1450.

[9] Kulatilaka, W. D., Naik, S. V., Lucht, R. P., "Development of High-Spectral Resolution Planar Laser-induced Fluorescence Imaging Diagnostics for High-Speed Gas Flow," *AIAA Journal*, Vol. 46, No. 1, 2008, pp. 17-20. doi: 10.2514/1.34971.
[10] Naik, S. V., Kulatilaka, W. D., Venkatesan, K. K., Lucht, R. P., "Measurements of Pressure, Temperature, and Velocity in Underexpanded Jets Using Laser-induced Fluorescence Imaging," *AIAA Journal*, Vol. 47, No. 4, 2009, pp. 839-849. doi: 10.2514/1.37343.
[11] Wang S., Hanson, R. K., "Quantitative 2-D OH thermometry using spectrally-resolved planar laser-induced fluorescence," *Optics Letters*, Vol. 44, No. 3, 2019, pp. 578-581. doi: 10.1364/OL.44.000578.
[12] Slipchenko, M. N., Meyer, T. R., Roy, S., "Advances in burst-mode laser diagnostics for reacting and nonreacting flows," *Proceedings of the Combustion Institute*, Vol. 38, No. 1, 2021, pp. 1533-1560. doi: 10.1016/j.proci.2020.07.024.
[13] Eckbreth, A. C., *Laser Diagnostics for Combustion Temperature and Species*, 2nd ed., Overseas Publishers Association, Amsterdam, 1996, Chap. 7.
[14] DiRosa, M. D., "High-resolution line shape spectroscopy of transitions in the gamma bands of nitric oxide," Ph.D. Dissertation, Stanford Univ., Stanford, California, 1996.
[15] Palma, P. C., "Laser-Induced Fluorescence Imaging in Free-Piston Shock Tunnels," Ph.D. Dissertation, Australian National Univ., Acton, Australia, 1999.
[16] Foo K. K., Lamoureux, N., Cessou, A., Lacour, C., Desgroux, P., "The accuracy and precision of multi-line NO-LIF thermometry in a wide range of pressures and temperatures", Journal of Quantitative Spectroscopy and Radiation Transfer, Vol. 255, 107257, 2020. doi: 10.1016/j.jqsrt.2020.107257
[17] Hsu, P. S., Jiang, N., Felver, J. J., Lauriola, D. K., Danehy P. M., "10 kHz two-color OH PLIF thermometry using a single burst-mode OPO," *Optics Letters*, Vol. 46, No. 10, 2021, pp. 2308-2311. doi: 10.1016/j.jqsrt.2020.107257.
[18] Hsu, P. S., Jiang, N., Lauriola, D. K., Roy, S., Danehy, P. M., "10-kHz PLIF Thermometry for a Turbulent Jet Flame using Single Burst-mode OPO", AIAA SCITECH 2022 Forum, January 2022. doi: 10.2514/6.2022-1523.
[19] Luque, J., Crosley, D. R., "LIFBASE: Database and Spectral Simulation Program (Version 1.5)," SRI International Report MP 99-009, 1999.
[20] Ashkenas, H., Sherman, F. S., "Structure and utilization of supersonic free jets in low density wind tunnels," No. NASA-CR-60423, 1965.